A comprehensive analysis of ^{19}F + ^{9}Be, ^{12}C, ^{16}O, ^{19}F, ^{27}Al, ^{28,30}Si, ^{40}Ca, ^{54,56}Fe, ^{208}Pb, ^{232}Th fusion reactions

M. Aygun and H. Cin

Department of Physics, Bitlis Eren University, Bitlis, Turkey.

Received 5 July 2021; accepted 30 October 2021

We theoretically analyze many fusion experimental data by using ten different density distributions of the ^{19}F nucleus. The real potentials are obtained by means of the double folding model while the imaginary potentials are established as the Woods-Saxon potential. The theoretical results are compared with the results calculated over one-dimensional Wong formula as well as the experimental data. Thus, alternative density distributions are proposed for the analysis of the experimental data of the ^{19}F fusion reactions. Additionally, the barrier positions and heights of all the analyzed fusion reactions are calculated for all the density distributions and new analytical expressions for these results are derived. Finally, new pocket formulas giving the imaginary potential depths for fusion cross-section calculations with ^{19}F are obtained for the first time.

Keywords: Fusion reaction reaction; density distribution; optical model; double folding model.

DOI: https://doi.org/10.31349/RevMexFis.68.031202

1. Introduction

The fusion reaction is a reaction where light nuclei can form a heavier nucleus. If the two interacting nuclei cross the Coulomb barrier, the fusion reaction can occur. The fusion reaction is one of the reactions studied to obtain information about the structure and properties of interacting nuclei. Thus, a lot of experimental and theoretical studies have been carried out [1, 2]. However, fusion reactions still deserve to be studied in the field of nuclear physics.

^{19}F is an important nucleus that has been extensively studied both experimentally and theoretically in the context of fusion reactions. In this context, the ^{19}F + ^{9}Be fusion cross section was reported at energies above the Coulomb barrier [3]. The experimental data of ^{19}F + ^{12}C fusion reaction was measured by Ref. [3]. They also investigated the effect of breakup on the fusion reaction, and reported that breakup has not an important influence. Anjos *et al.* [4] reported the fusion cross-section of ^{19}F + ^{16}O system. They showed that the light heavy-ion fusion cross-sections depended on the entrance channel mass asymmetry. The fusion data of ^{19}F + ^{19}F reaction was measured by Ref. [4]. The ^{19}F + ^{27}Al fusion experimental data was presented by Ref. [3]. Chiou et al. [5] recorded the cross-sections of ^{19}F + ^{28,30}Si fusion reactions, and compared the data with the theoretical results obtained using different models. The fusion data of ^{19}F + ^{40}Ca reaction was reported by Ref. [4]. The experimental data of ^{19}F + ^{54,56}Fe fusion reactions were measured by Ref. [6]. They observed that the one-dimensional barrier penetration model did not successfully explain the data. Then, they performed the coupled channel calculations, and obtained agreement results with the experimental data. The fusion experimental data of ^{19}F + ^{208}Pb was reported by Ref. [7]. Finally, the fusion data of ^{19}F + ^{232}Th system was measured [8]. We have noticed from these studies that the effect of different density distributions on the ^{19}F fusion cross-sections has not yet been examined simultaneously.

The nuclear potential is one of the parameters required to explain fusion reactions. With the help of this potential, an accurate analysis of the system can be performed. The double folding model (DFM) is one of the widely used models for this purpose [9–11]. It uses the density distributions of the projectile and target nuclei. Therefore, the density distribution is of particular importance in generating the nuclear potential. Recently, Aygun [12] examined the effect of different density distributions of ^{19}F on the elastic scattering cross-sections, and obtained good agreement results with the experimental data. We believe that it would be important and useful to see the effectiveness of these density distributions on the ^{19}F fusion cross-sections.

In the present study, we first calculate the cross-sections of ^{19}F + ^{9}Be, ^{19}F + ^{12}C, ^{19}F + ^{16}O, ^{19}F + ^{19}F, ^{19}F + ^{27}Al, ^{19}F + ^{28}Si, ^{19}F + ^{30}Si, ^{19}F + ^{40}Ca, ^{19}F + ^{54}Fe, ^{19}F + ^{56}Fe, ^{19}F + ^{208}Pb and ^{19}F + ^{232}Th fusion reactions by using ten different density distributions of ^{19}F. Then, we obtain the fusion cross-sections based on the one-dimensional Wong formula in order to make a comparative study. We compare our results with the one-dimensional Wong results as well as the experimental data. Then, we calculate the barrier positions (R_B) and heights (V_B) for all the analyzed fusion reactions and the density distributions, and derive new analytical expressions for these results. Finally, we acquire for the first time global potential equations that provide the imaginary potential depths for all the analyzed density distributions.

Section 2 presents the calculation procedure which consists of the models and densities. Section 3 states the results and discussion. Section 4 gives the summary and conclusions.

2. Calculation procedure

2.1. Optical model

The optical model possesses two potentials: one real and one imaginary. The DFM produces the real part of the optical model by means of the following equation

$$V(\overrightarrow{r}) = \int d\overrightarrow{r}_1 \int d\overrightarrow{r}_2 \rho_P(\overrightarrow{r}_1)\rho_T(\overrightarrow{r}_2)\nu_{NN}(\overrightarrow{r} - \overrightarrow{r}_1 + \overrightarrow{r}_2), \tag{1}$$

where $\rho_{P(T)}(\overrightarrow{r}_{1(2)})$, respectively are the densities of projectile and target, and ν_{NN} is nucleon-nucleon interaction accepted as [13]

$$\nu_{NN}(r) = 7999\,\frac{\exp(-4r)}{4r} - 2134\,\frac{\exp(-2.5r)}{2.5r} - \,276\,\left(1 - 0.005\frac{E_{\rm Lab}}{A_p}\right)\,\delta(r)\ \text{MeV}. \tag{2}$$

The imaginary part of the optical model is taken in the Woods-Saxon type

$$W(r) = -\frac{W_0}{1+\exp\left(\frac{r-R_w}{a_w}\right)}, \qquad R_w = r_w\,(A_P^{1/3} + A_T^{1/3}), \tag{3}$$

where W_0 is the depth, r_w is the radius, and a_w is diffuseness parameter. The code DFPOT [14] is applied in the DFM calculations.

2.2. Fusion cross-sections

In this study, the fusion cross-sections are calculated by using the code FRESCO [15] based on the barrier penetration model (BPM). Within the framework of the BPM, the fusion cross-section can be written in the following form

$$\sigma_{Fus}(E) = \frac{\pi}{k^2}\sum_{\ell=0}^{\infty}(2\ell+1)T_\ell(E). \tag{4}$$

$T_l(E)$ is the transmission coefficient, and is given as

$$T_\ell(E) = 1 - |S_\ell|^2, \tag{5}$$

where S_ℓ is S-matrix. $T_l(E)$ value is acquired over numerical integration of the following Schrödinger equation [2]

$$\frac{d^2u_l(r)}{dr^2} + \frac{2\mu}{\hbar^2}\left[E - V_{total}(r)\right]u_l(r) = 0. \tag{6}$$

2.3. Densities of ^{19}F projectile

2.3.1. São Paulo (SP), Fermi (2pF), Schechter (S), Moszkowski (M), Jager (J)

SP [16], 2pF [17], S [18], M [19] and J [20] densities can be taken as the two parameter Fermi

$$\rho_i(r) = \frac{\rho_{0i}}{1+\exp\left(\frac{r-R_i}{a_i}\right)}, \quad (i = n, p), \tag{7}$$

where ρ_{0i}, R_i and a_i parameters are listed in Table I.

TABLE I. The ρ_0, R_0 and a values of SP, 2pF, S, M and J densities.

Density	ρ_0 (fm^{-3})	R_0 (fm)	a (fm)	Ref.
SP	ρ_{0n}=0.1220860	R_n=2.42011	a_n=0.47460	[16]
	ρ_{0p}=0.0891972	R_p=2.64495	a_p=0.46253	
2pF	ρ_{0n}=0.0700497	R_n=2.96218	a_n=0.526	[17]
	ρ_{0p}=0.0708402	R_p=2.84187	a_p=0.5129	
S	0.154342	2.77514	0.54	[18]
M	0.16	3.06866	0.50	[19]
J	0.17784	2.59	0.564	[20]

2.3.2. Ngô (Ngo)

Ngo density can be formulated as [21, 22]

$$\rho_{n(p)}(r) = \frac{\frac{3}{4\pi}\frac{N(Z)}{A}\frac{1}{r^3_{0n(0p)}}}{1+\exp\left(\frac{r-C}{0.55}\right)}, \qquad C = R(1-\frac{1}{R^2}), \tag{8}$$

where

$$R = \frac{Nr_{0n}A^{1/3} + Zr_{0p}A^{1/3}}{A}, \qquad r_{0n} = 1.1375 + 1.875\times10^{-4}A, \qquad r_{0p} = 1.128\,\text{fm}. \tag{9}$$

2.3.3. Gupta 1 (G1)

G1 density [23, 24] is given by

$$\rho_i(r) = \frac{\rho_{0i}}{1+\exp\left(\frac{r-R_{0i}}{a_i}\right)}, \qquad \rho_{0i} = \frac{3A_i}{4\pi R^3_{0i}}\left(1+\frac{\pi^2a_i^2}{R^2_{0i}}\right)^{-1}, \tag{10}$$

where

$$R_{0i} = 0.90106 + 0.10957A_i - 0.0013A_i^2 + 7.71458\times10^{-6}A_i^3 - 1.62164\times10^{-8}A_i^4, \tag{11}$$

$$a_i = 0.34175 + 0.01234A_i - 2.1864\times10^{-4}A_i^2 + 1.46388\times10^{-6}A_i^3 - 3.24263\times10^{-9}A_i^4. \tag{12}$$

2.3.4. Gupta 2 (G2)

G2 density [25] based on Eq. (10) is accepted as

$$R_{0i} = 0.9543 + 0.0994A_i - 9.8851\times10^{-4}A_i^2 + 4.8399\times10^{-6}A_i^3 - 8.4366\times10^{-9}A_i^4, \tag{13}$$

$$a_i = 0.3719 + 0.0086A_i - 1.1898\times10^{-4}A_i^2 + 6.1678\times10^{-7}A_i^3 - 1.0721\times10^{-9}A_i^4. \tag{14}$$

2.3.5. Wesolowski (W)

W density [26] is in the following form [27]

$$\rho_0 = \frac{3}{4\pi R_0^3}\left(1+\frac{\pi^2a^2}{R_0^2}\right)^{-1}, \qquad a = 0.39\,\text{fm}, \tag{15}$$

$$R_0 = R^{'}\left[1-(\frac{b}{R^{'}})^2 + \frac{1}{3}(\frac{b}{R^{'}})^6 + ...\right], \tag{16}$$

$$R^{'} = \left[1.2 - \frac{0.96}{A^{1/3}}\left(\frac{N-Z}{A}\right)\right]A^{1/3}, \qquad b = \frac{\pi}{\sqrt{3}}a. \tag{17}$$

2.3.6. Hartree-Fock-Bogolubov (HFB)

Neutron and proton densities are obtained over the HFB model considering the BSk2 Skyrme force calculations [28]. In this respect, detailed information about the BSk2 force and the HFB model can be found from Refs. [29] and [30], respectively.

2.4. Densities of target nuclei

In our study, the ^{9}Be density is taken as [31]

$$\rho(r) = (A+BC^2r^2)\text{exp}(-C^2r^2) + (D+EF^2r^2)\text{exp}(-F^2r^2), \tag{18}$$

where $A = 0.0651$, $B = 0.0398$, $C = 0.5580$, $D = 0.0544$, $E = 0.0332$, and $F = 0.4878$.

The densities of ^{12}C and ^{16}O targets are produced by

$$\rho(r) = (\xi+\gamma r^2)\exp(-\beta r^2), \tag{19}$$

where ξ=0.1644, γ=0.082003, β=0.3741 for ^{12}C [32], and ξ=0.13173, γ=0.085058, β=0.3228 for ^{16}O [33–35].

TABLE II. The 2pF density parameters for ^{27}Al, ^{28}Si, ^{30}Si, ^{40}Ca, ^{54}Fe, ^{56}Fe, ^{208}Pb and ^{232}Th targets.

Nucleus	ρ_0 (fm^{-3})	c (fm)	z (fm)	Ref.
^{27}Al	0.2015	2.84	0.569	[36]
^{28}Si	0.175	3.15	0.475	[32]
^{30}Si	0.174908	3.17048	0.538603	[25]
^{40}Ca	0.169	3.60	0.523	[32]
^{54}Fe	0.1699279	4.012	0.5339	[20]
^{56}Fe	0.174934	3.971	0.5935	[20]
^{208}Pb	0.1600	6.62	0.551	[36]
^{232}Th	0.16477	6.80516	0.559058	[25]

TABLE III. The imaginary potential depths (W_0) obtained from the analysis of the fusion reactions. The geometrical parameters are fixed as follows: r_w= 1.07 fm and a_w = 0.75 fm.

Reaction	SP	2pF	Ngo	G1	G2	W	S	M	J	HFB
^{19}F + ^{9}Be	2.60	2.20	2.20	2.50	2.60	2.50	2.20	2.15	2.25	2.45
^{19}F + ^{12}C	16.5	7.50	7.50	12.5	14.0	11.2	8.20	7.50	8.90	11.0
^{19}F + ^{16}O	4.80	3.30	3.30	4.00	4.10	4.30	3.30	3.10	3.30	3.90
^{19}F + ^{19}F	7.50	3.20	3.50	5.50	6.20	6.50	3.20	3.20	3.40	4.80
^{19}F + ^{27}Al	4.20	2.70	2.80	3.50	3.55	3.70	2.80	2.70	2.80	3.20
^{19}F + ^{28}Si	4.00	2.60	2.70	3.60	3.80	3.60	2.70	2.60	2.70	3.20
^{19}F + ^{30}Si	3.70	2.70	2.70	3.50	3.80	3.60	3.20	2.70	2.70	3.30
^{19}F + ^{40}Ca	8.50	3.70	4.50	7.60	7.00	7.30	4.00	3.60	4.00	5.00
^{19}F + ^{54}Fe	2.80	1.40	1.45	2.10	2.30	2.30	1.40	1.35	1.50	2.10
^{19}F + ^{56}Fe	2.20	1.10	1.10	1.60	1.90	2.10	1.10	1.10	1.20	1.50
^{19}F + ^{208}Pb	9.00	6.00	6.00	7.60	8.00	9.00	6.00	6.00	7.00	8.00
^{19}F + ^{232}Th	17.5	9.50	9.50	17.0	17.0	16.5	9.50	8.50	9.50	15.5

The density distributions of ^{27}Al, ^{28}Si, ^{30}Si, ^{40}Ca, ^{54}Fe, ^{56}Fe, ^{208}Pb and ^{232}Th targets are accepted as the 2pF density shown by

$$\rho(r) = \frac{\rho_0}{1 + \exp\left(\frac{r-c}{z}\right)}, \tag{20}$$

where ρ_0, c and z parameters are given in Table II.

3. Results and Discussion

3.1. Fusion cross-sections

The fusion cross-sections have been calculated for ten different densities of the ^{19}F nucleus that includes SP, 2pF, Ngo, G1, G2, W, S, M, J and HFB. The changes with the distance of the density distributions can be found in our previous work [12]. While the real parts of the optical model potential are obtained using these density distributions, the imaginary parts are assumed as the Woods-Saxon potential. In order to acquire good agreement results with the experimental data, the depth (W_0), radius (r_w) and diffussenes (a_w) parameters of the Woods-Saxon potential are researched at 0.1 and 0.01 step intervals. Additionally, the same potential geometry for all reactions is applied to obtain general expressions of the imaginary potentials. Thus, the r_w and a_w values are accepted as 1.07 fm and 0.75 fm, respectively. Finally, the W_0 values which are determined at the values of r_w and a_w are given in Table III.

The cross-section calculations have been carried out for light, medium and heavy mass targets. For light mass targets, we have analyzed the ^{19}F + ^{9}Be, ^{19}F + ^{12}C, ^{19}F + ^{16}O, ^{19}F + ^{19}F, ^{19}F + ^{27}Al, ^{19}F + ^{28}Si and ^{19}F + ^{30}Si fusion reactions. We have presented the theoretical results for ^{19}F + ^{9}Be in Fig. 1, ^{19}F + ^{12}C in Fig. 2, for ^{19}F + ^{16}O in Fig. 3, for ^{19}F + ^{19}F in Fig. 4, for ^{19}F + ^{27}Al in Fig. 5, for ^{19}F + ^{28}Si in Fig. 6 and for ^{19}F + ^{30}Si in Fig. 7. In the ^{19}F + ^{9}Be, the results of the density distributions show similar results with each other, and agree with the data. We have observed that

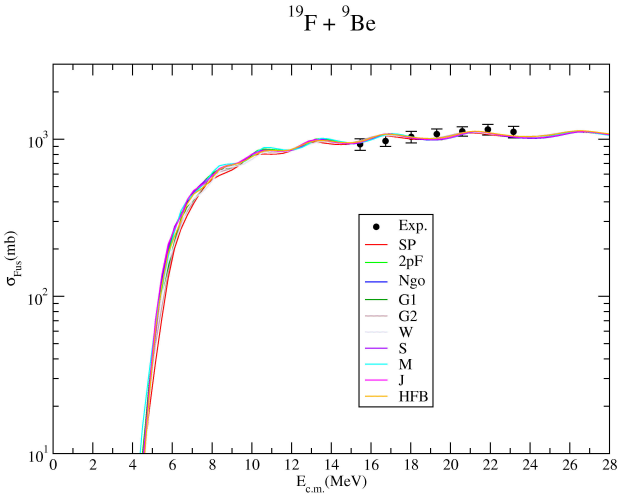

FIGURE 1. The fusion cross-sections ^{19}F + ^{9}Be system calculated by using different densities of the ^{19}F nucleus in comparison with the experimental data [37].

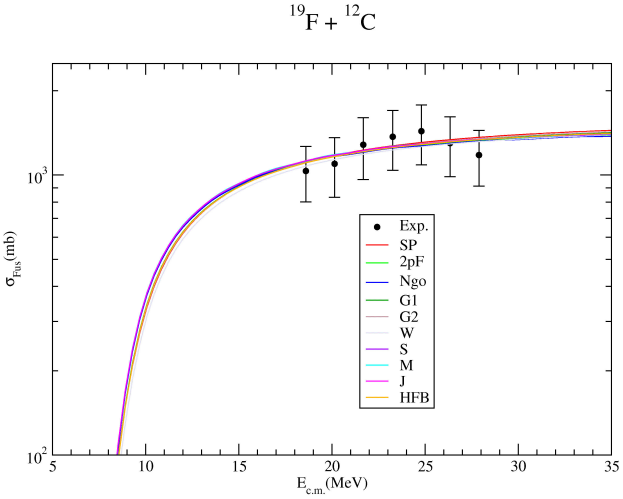

FIGURE 2. Same as Fig. 1, but for ^{19}F + ^{12}C reaction. The data are from Ref. [37].

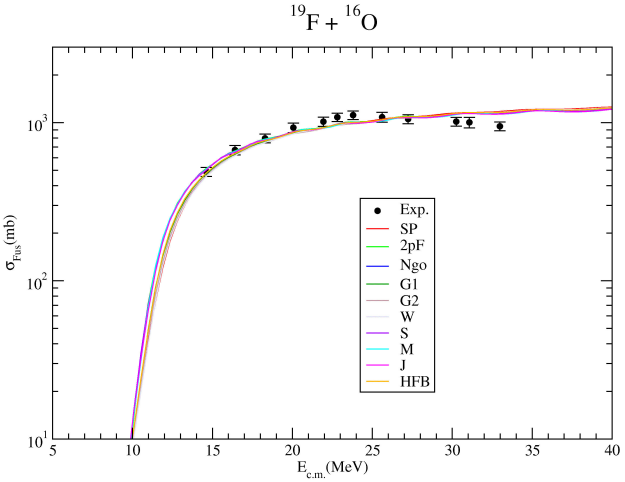

FIGURE 3. Same as Fig. 1, but for ^{19}F + ^{16}O reaction. The data are from Ref. [37].

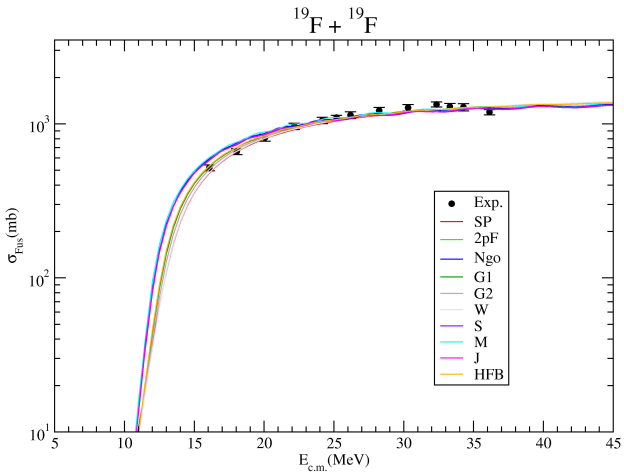

FIGURE 4. Same as Fig. 1, but for ^{19}F + ^{19}F reaction. The data are from Ref. [37].

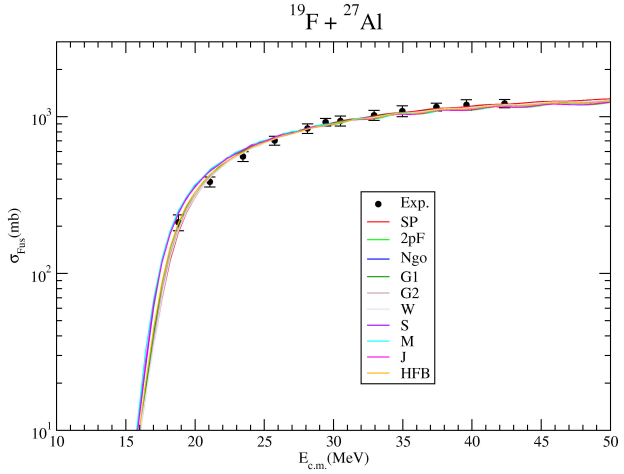

FIGURE 5. Same as Fig. 1, but for ^{19}F + ^{27}Al reaction. The data are from Ref. [37].

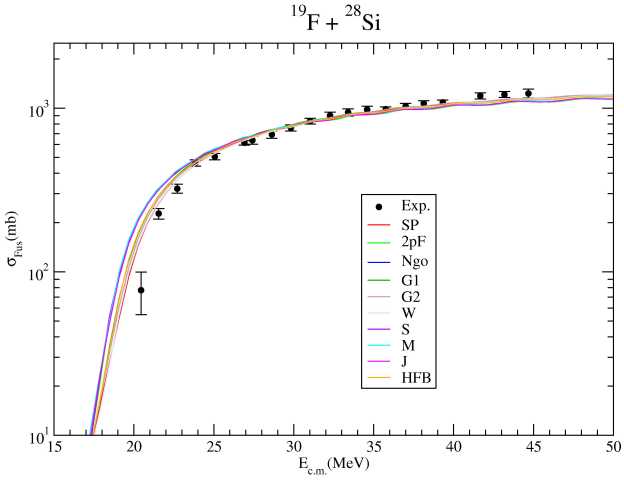

FIGURE 6. Same as Fig. 1, but for ^{19}F + ^{28}Si reaction. The data are from Ref. [37].

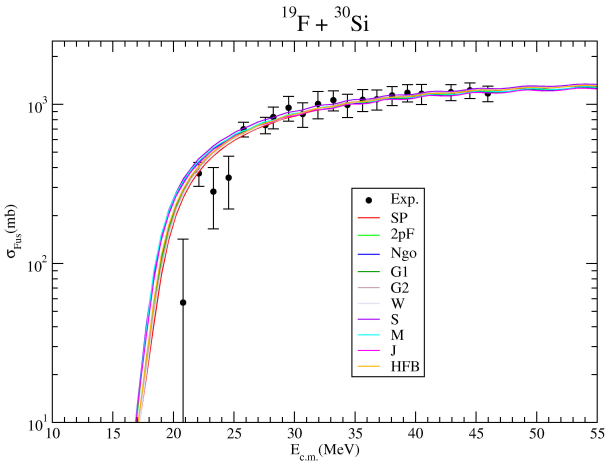

FIGURE 7. Same as Fig. 1, but for ^{19}F + ^{30}Si reaction. The data are from Ref. [37].

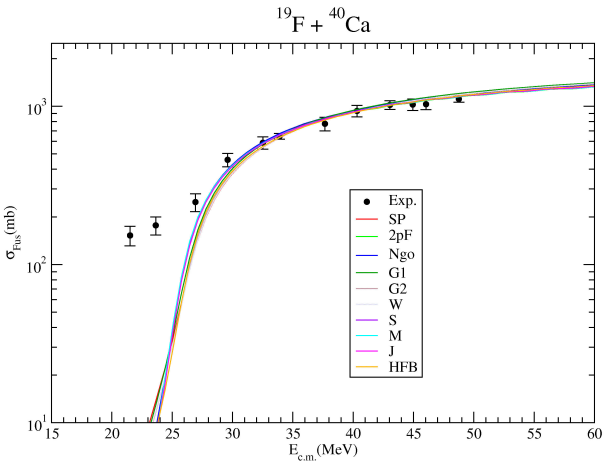

FIGURE 8. Same as Fig. 1, but for ^{19}F + ^{40}Ca reaction. The data are from Ref. [37].

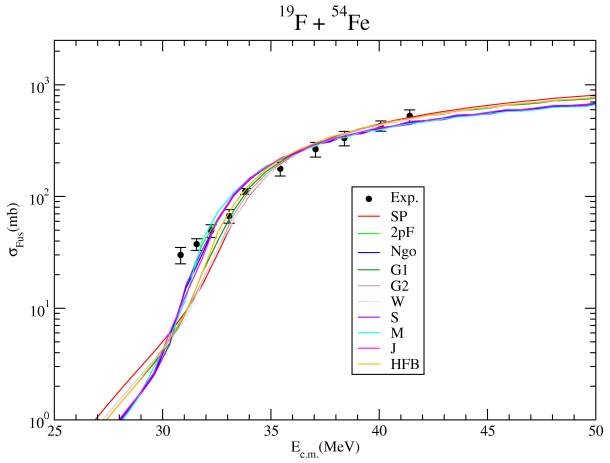

FIGURE 9. Same as Fig. 1, but for ^{19}F + ^{54}Fe reaction. The data are from Ref. [37].

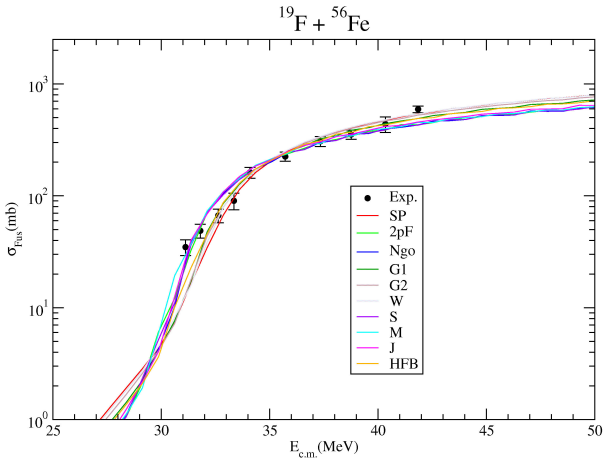

FIGURE 10. Same as Fig. 1, but for ^{19}F + ^{56}Fe reaction. The data are from Ref. [37].

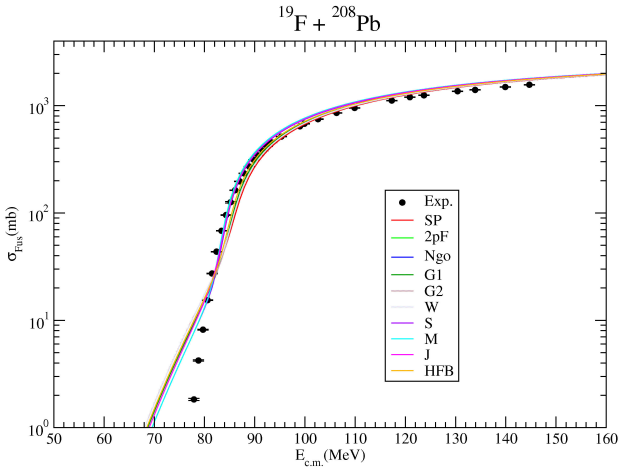

FIGURE 11. Same as Fig. 1, but for ^{19}F + ^{208}Pb reaction. The data are from Ref. [37].

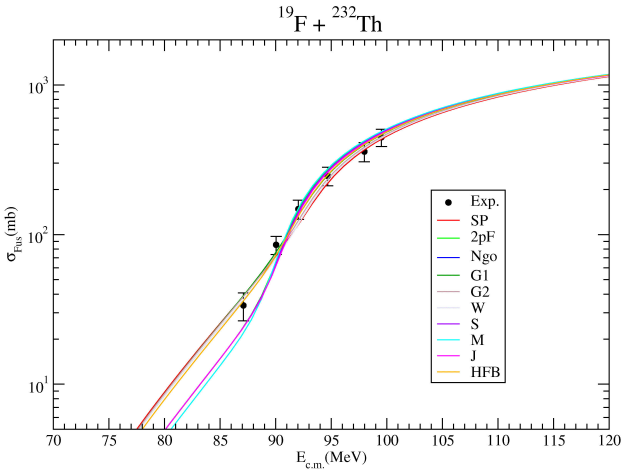

FIGURE 12. Same as Fig. 1, but for ^{19}F + ^{232}Th reaction. The data are from Ref. [37].

the density results of ^{19}F + ^{12}C exhibit similar results with each other, and are in good agreement with the experimen-

tal data (within the error limits). For ^{19}F + ^{16}O reaction, we have noticed that the density distributions are coherent with the data. We have observed that the results of the ^{19}F + ^{19}F and ^{19}F + ^{27}Al reactions are in good agreement with the experimental data. At the same time, it has been observed that there is a slight difference in the results at small energies. In the ^{19}F + ^{28}Si reaction, it has been seen that the density distributions fit well the experimental data, and the SP and W densities are slightly better than the other densities. In the ^{19}F + ^{30}Si reaction, it has been observed that the SP, G1, G2, and HFB results match the experimental data very well. Additionally, it can be said that low energy results, which cannot define the data, have very high experimental error values. Consequently, it can be expressed that the results obtained using the density distributions can explain well the experimental data of ^{19}F + ^{9}Be, ^{19}F + ^{12}C, ^{19}F + ^{16}O, ^{19}F + ^{19}F, ^{19}F + ^{27}Al, ^{19}F + ^{28}Si and ^{19}F + ^{30}Si fusion reactions, and these density distributions can be evaluated for the theoretical analysis of ^{19}F fusion reactions.

We have investigated the ^{19}F + ^{40}Ca, ^{19}F + ^{54}Fe and ^{19}F + ^{56}Fe systems as fusion reactions with medium mass targets. We have compared our results together with the experimental data of ^{19}F + ^{40}Ca in Fig. 8, ^{19}F + ^{54}Fe in Fig. 9 and ^{19}F + ^{56}Fe in Fig. 10. For the ^{19}F + ^{40}Ca reaction, we have observed that the agreement between the theoretical results and the experimental data is good. In the ^{19}F + ^{54}Fe reaction, we have noticed that the theoretical results are in good agreement with the data. For the ^{19}F + ^{56}Fe reaction, we have observed that 2pF, Ngo, S, M and J densities are slightly better than the other densities although the densities fit the data well.

As the fusion reacts with heavy mass targets, we have analyzed the ^{19}F + ^{208}Pb and ^{19}F + ^{232}Th systems. We have presented the theoretical results of ^{19}F + ^{208}Pb in Fig. 11 and ^{19}F + ^{232}Th in Fig. 12. For the ^{19}F + ^{208}Pb and ^{19}F + ^{232}Th reactions, we have observed that the density distributions show an average behavior with the experimental data. It has been seen that the densities for ^{19}F + ^{208}Pb reaction behave close to each other. Additionally, it has been realized that the HFB density for ^{19}F + ^{232}Th reaction is slightly more compatible with the experimental data compared to the other densities.

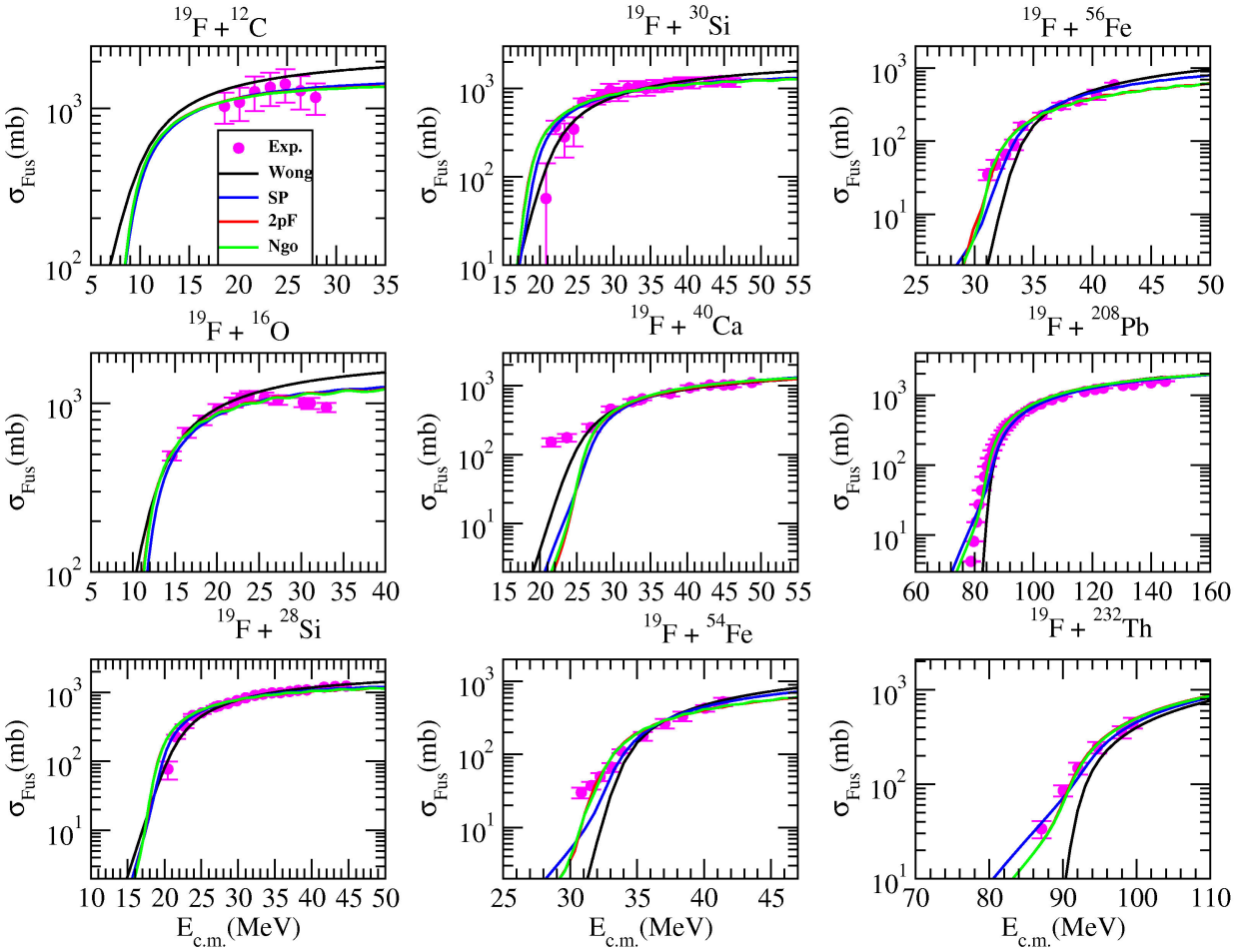

FIGURE 13. A comparison of the ^{19}F + ^{12}C, ^{19}F + ^{16}O, ^{19}F + ^{28}Si, ^{19}F + ^{30}Si, ^{19}F + ^{40}Ca, ^{19}F + ^{54}Fe, ^{19}F + ^{56}Fe, ^{19}F + ^{208}Pb and ^{19}F + ^{232}Th fusion cross-sections calculated by means of SP, 2pF and Ngo densities and one-dimensional Wong formula.

TABLE IV. The R_B (in fm), V_B (in MeV) and $\hbar\,\omega$ (in MeV) values evaluated in calculating the ^{19}F + ^{12}C, ^{19}F + ^{16}O, ^{19}F + ^{28}Si, ^{19}F + ^{30}Si, ^{19}F + ^{40}Ca, ^{19}F + ^{54}Fe, ^{19}F + ^{56}Fe, ^{19}F + ^{208}Pb and ^{19}F + ^{232}Th fusion cross-sections by using one-dimensional Wong formula.

Reaction	R_B (fm)	V_B (MeV)	$\hbar\,\omega$ (MeV)	Ref.
^{19}F + ^{12}C	8.79	8.51	7.50	[4,40]
^{19}F + ^{16}O	8.23	11.21	7.50	[4,40]
^{19}F + ^{28}Si	8.72	20.33	7.50	[40]
^{19}F + ^{30}Si	8.91	20.41	7.50	[40]
^{19}F + ^{40}Ca	8.41	24.09	7.50	[4,40]
^{19}F + ^{54}Fe	9.43	33.20	3.70	[6]
^{19}F + ^{56}Fe	9.48	33.00	3.66	[6]
^{19}F + ^{208}Pb	11.8	84.50	4.50	[41]
^{19}F + ^{232}Th	11.92	91.07	4.25	[42]

TABLE V. The R_B (in fm) and V_B (in MeV) values calculated for SP, 2pF, Ngo, G1, G2, W, S, M, J and HFB densities together with the literature and experimental values for various fusion reactions.

Target	Parameter	SP	2pF	Ngo	G1	G2	W	S	M	J	HFB	Lit.	Exp.
^{9}Be	R_B	5.62	5.38	5.38	5.52	5.56	5.60	5.38	5.37	5.38	5.50		
	V_B	8.54	8.90	8.88	8.68	8.62	8.60	8.90	8.94	8.88	8.72		
^{12}C	R_B	8.06	8.44	8.42	8.20	8.14	8.12	8.44	8.48	8.42	8.26	8.79 [4]	
	V_B	8.93	8.51	8.51	8.76	8.82	8.91	8.51	8.49	8.51	8.73	8.51 [4]	
^{16}O	R_B	8.30	8.68	8.64	8.44	8.38	8.36	8.66	8.71	8.64	8.48	8.23 [4]	
	V_B	11.57	11.06	11.06	11.37	11.45	11.55	11.06	11.03	11.07	11.33	11.21 [4]	
^{19}F	R_B	8.34	9.06	9.02	8.62	8.50	8.46	9.04	9.14	9.00	8.70	8.30 [4]	
	V_B	12.92	11.86	11.88	12.48	12.65	12.86	11.87	11.80	11.90	12.40	12.44 [4]	
^{27}Al	R_B	8.82	9.16	9.14	8.94	8.88	8.88	9.14	9.20	9.12	8.98	8.40 [4]	9.06 [47]
	V_B	17.59	16.92	16.94	17.32	17.43	17.52	16.93	16.87	16.95	17.26	17.54 [4]	17.95 [47]
^{28}Si	R_B	8.68	9.04	9.02	8.82	8.76	8.74	9.02	9.08	9.00	8.86	8.72 [40]	9.05 [47]
	V_B	19.33	18.55	18.56	19.02	19.15	19.26	18.55	18.50	18.57	18.95	20.33 [40]	19.31 [47]
^{30}Si	R_B	8.94	9.28	9.26	9.06	9.02	9.00	9.28	9.32	9.24	9.10	8.91 [40]	9.18 [47]
	V_B	18.74	18.03	18.05	18.46	18.57	18.67	18.04	17.98	18.05	18.40	20.41 [40]	19.05 [47]
^{40}Ca	R_B	9.10	9.44	9.42	9.22	9.16	9.18	9.42	9.48	9.40	9.26	8.41 [4]	
	V_B	26.33	25.36	25.39	25.96	26.11	26.22	25.38	25.29	25.41	25.86	24.09 [4]	
^{54}Fe	R_B	9.44	9.78	9.74	9.56	9.50	9.52	9.76	9.82	9.72	9.60	9.43 [6]	
	V_B	33.06	31.90	31.94	32.61	32.80	32.92	31.92	31.81	31.96	32.49	33.2 [6]	
^{56}Fe	R_B	9.62	9.94	9.92	9.74	9.68	9.70	9.92	9.98	9.90	9.78	9.48 [6]	
	V_B	32.36	31.28	31.33	31.95	32.12	32.22	31.31	31.20	31.35	31.84	33.0 [6]	
^{208}Pb	R_B	11.60	11.90	11.88	11.70	11.66	11.68	11.88	11.96	11.86	11.76	11.80 [41]	11.25 [48]
	V_B	85.74	83.41	83.54	84.87	85.24	85.35	83.49	83.19	83.61	84.59	84.50 [41]	87.44 [48]
^{232}Th	R_B	11.80	12.10	12.06	11.90	11.84	11.88	12.08	12.14	12.04	11.94	11.92 [42]	11.46 [49]
	V_B	92.68	90.22	90.36	91.76	92.15	92.26	90.30	89.98	90.44	91.46	91.07 [42]	89.50 [49]

3.2. One-dimensional Wong formula

To make a comparative study, we have calculated the fusion cross-sections within the scope of one-dimensional Wong formula. In order to obtain the results, we have applied the Wong formula [38] in the following form

$$\sigma(E) = \frac{\hbar\omega {R_b}^2}{2E} \log\left\{1 + \exp\left[\frac{2\pi}{\hbar\omega}\left(E - V_b\right)\right]\right\}, \quad (21)$$

where V_b, R_b and $\hbar\omega$, respectively are the barrier height, radius and curvature [39] which are listed in Table IV. In order

to make a comparative study, we have obtained the Wong formula results for ^{19}F + ^{12}C, ^{19}F + ^{16}O, ^{19}F + ^{28}Si, ^{19}F + ^{30}Si, ^{19}F + ^{40}Ca, ^{19}F + ^{54}Fe, ^{19}F + ^{56}Fe, ^{19}F + ^{208}Pb and ^{19}F + ^{232}Th fusion reactions. Then, we have compared the Wong with some density distributions which provides good agreement results with the experimental data in Fig. 13. We have noticed that the results are better than the Wong results in general.

3.3. Barrier position (R_B) and height (V_B) values

The R_B and V_B are among the desired parameters to be known by the analysis of fusion reactions. For this purpose, we have calculated the R_B and V_B values for all the density distributions and all the fusion reactions investigated with this study. The R_B and V_B values can be determined from the analytical form of the total interaction potential. From this point of view, we obtain the R_B and V_B parameters from the total potential based on the potential parameters used in the theoretical calculations. We have listed our results together with experimental and literature values in Table V. We have observed that our results are consistent with the literature.

It is helpful to formulate the R_B and V_B parameters calculated in the theoretical analysis of fusion reactions. As known from the literature [3, 38, 43–46], the R_B depends on the size of the colliding systems. Thus, the Eq. (22) can be obtained when the R_B is fitted in the context of $(A_P^{1/3}+A_T^{1/3})$ terms. Additionally, V_B parameter is linearly dependent on the $(Z_P + Z_T)/(A_P^{1/3} + A_T^{1/3})$ term, and Eq. (23) can be acquired for the V_B. Thus, new analytical expressions of the R_B and V_B parameters can be written in the following form

$$R_B = 1.14093(A_P^{1/3} + A_T^{1/3}) + 2.0083 \quad \text{fm}, \tag{22}$$

$$V_B = 1.02636\frac{Z_P Z_T}{A_P^{1/3} + A_T^{1/3}} - 2.85701 \quad \text{MeV}. \tag{23}$$

3.4. New pocket formulas of the imaginary potential

It is useful to determine the potential parameters used in the theoretical analysis of fusion reactions. A pocket formula giving the imaginary potential depth would be helpful in describing the fusion cross-sections by using the DFM. We have realized that such an equation is absent for these densities when we have examined the fusion reactions with the ^{19}F nucleus. To obtain a pocket formula for the W_0 values determined using the density distributions, we have used the same potential geometry accepted for all the reaction and the densities as well as the W_0 values given in Table III. In this context, the equations should depend on the W_0 values together with the charge (Z_T) and the mass (A_T) numbers of the target. So the Eqs. (24)-(33) can be obtained by fitting the W_0 values given in Table III at r_w = 1.07 fm and $a_w = 0.75$ fm values. We would like to point out here that we do not get precise expressions. We simply propose new equations that give their imaginary potential depths by taking a different approach to the analysis of fusion reactions. Thus, we have acquired for the first time ten different potential equations for ten different densities by using the potential parameters that are determined in the cross-section calculations. These equations are formulated as

$$\text{SP density} \Rightarrow W^{SP} = 3.61 + \frac{0.55Z_T}{A_T^{1/3}}, \tag{24}$$

$$\text{2pF density} \Rightarrow W^{2pF} = 1.75 + \frac{0.34Z_T}{A_T^{1/3}}, \tag{25}$$

$$\text{Ngo density} \Rightarrow W^{Ngo} = 1.90 + \frac{0.34Z_T}{A_T^{1/3}}, \tag{26}$$

$$\text{G1 density} \Rightarrow W^{G1} = 2.34 + \frac{0.59Z_T}{A_T^{1/3}}, \tag{27}$$

$$\text{G2 density} \Rightarrow W^{G2} = 2.77 + \frac{0.57Z_T}{A_T^{1/3}}, \tag{28}$$

$$\text{W density} \Rightarrow W^{W} = 2.22 + \frac{0.63Z_T}{A_T^{1/3}}, \tag{29}$$

$$\text{S density} \Rightarrow W^{S} = 2.00 + \frac{0.32Z_T}{A_T^{1/3}}, \tag{30}$$

$$\text{M density} \Rightarrow W^{M} = 1.88 + \frac{0.30Z_T}{A_T^{1/3}}, \tag{31}$$

$$\text{J density} \Rightarrow W^{J} = 1.96 + \frac{0.35Z_T}{A_T^{1/3}}, \tag{32}$$

$$\text{HFB density} \Rightarrow W^{HFB} = 1.76 + \frac{0.59Z_T}{A_T^{1/3}}, \tag{33}$$

where Z_T and A_T are atomic and mass numbers of target, respectively. We would like to point out that these equations are approximate expressions.

4. Summary and Conclusions

We have analyzed the cross-sections of ^{19}F + ^{9}Be, ^{19}F + ^{12}C, ^{19}F + ^{16}O, ^{19}F + ^{19}F, ^{19}F + ^{27}Al, ^{19}F + ^{28}Si, ^{19}F + ^{30}Si, ^{19}F + ^{40}Ca, ^{19}F + ^{54}Fe, ^{19}F + ^{56}Fe, ^{19}F + ^{208}Pb and ^{19}F + ^{232}Th fusion reactions by using ten type densities of the ^{19}F nucleus. We have obtained good agreement with the experimental data. Thus, we have proposed alternative density distributions for the theoretical analysis of the ^{19}F fusion reactions.

In the present study, we have also calculated the R_B and V_B values for all the density distributions and all the fusion reactions. Additionally, we have derived new equations which give the R_B and V_B parameters.

Finally, we have produced new and practical pocket formulas of imaginary potentials for ten different densities of the ^{19}F nucleus. We believe that the formulas would be helpful in understanding the mechanism of fusion reactions induced by the ^{19}F nucleus.

Acknowledgements

The authors would like to thank the referee for useful comments.

1. M. Aygun and Z. Aygun, A comprehensive analysis of 9Li +70 Zn fu- sion cross section by using proximity potentials, temperature dependent den- sity distributions and nuclear potentials, *Rev. Mex. Fis.* **65** (2019) 573, https://doi.org/10.31349/revmexfis.65.573.
2. G. Kocak, M. Aygun, A theoretical analysis of the cross sections of 18;19;20O +12 C fusion reactions by using different density distributions, *Nucl. Phys. A* **1003** (2020) 122015, https://doi.org/10.1016/j.nuclphysa.2020.122015.
3. R. M. Anjos *et al.*, No evidence of break-up effects on the fusion of 9Be with medium-light nuclei, *Phys. Lett. B* **534** (2002) 45, https://doi.org/10.1016/S0370-2693(02)01554-X.
4. R. M. Anjos *et al.*, Effect of the entrance channel mass asymmetry on the limitation of light heavy-ion fusion cross sections, *Phys. Rev. C* **42** (1990) 354, https://doi.org/10.1103/PhysRevC.42.354.
5. M. S. Chiou, M. W. Wu, N. Easwar and J. V. Maher, Complete fusion of 19F with Al and Si isotopes, *Phys. Rev. C* **24** (1981) 2507, https://doi.org/10.1103/PhysRevC.24.2507.
6. H. Funaki and E. Arai, Anomaly in the 15N, 16O, 19F +54;56 Fe fusion cross sections around the Coulomb barrier energy, *Nucl. Phys. A* **556** (1993) 307, https://doi.org/10.1016/0375-9474(93)90353-Y.
7. D. J. Hinde, A. C. Berriman, M. Dasgupta, J. R. Leigh, J. C. Mein, C. R. Morton and J. O. Newton, Limiting angular momentum for statistical model de- scription of fission, *Phys. Rev. C* **60** (1999) 054602, https://doi.org/10.1103/PhysRevC.60.054602.
8. S. Kailas *et al.*, Fission fragment angular distributions for the system 19F+232Th, *Phys. Rev. C* **43** (1991) 1466, https://doi.org/10.1103/PhysRevC.43.1466.
9. Z. Gao-Long and L. Xiao-Yun, Double folding model calculation applied to fusion reactions, *Chin. Phys. C* **32** (2008) 812, https://doi.org/10.1088/1674-1137/32/10/009.
10. I. I. Gontchar, D. J. Hinde, M. Dasgupta and J. O. Newton, Double fold- ing nucleus-nucleus potential applied to heavy-ion fusion reactions, *Phys. Rev. C* **69** (2004) 024610, https://doi.org/10.1103/PhysRevC.69.024610.
11. M. Rashdan, Folding model description of 16O+154Sm fusion reaction, *J. Phys. G: Nucl. Part. Phys.* **22** (1996) 139, https://doi.org/10.1088/0954-3899/22/1/013.
12. M. Aygun, A Comprehensive Description of 19F Elastic Scattering by 12C, 16O, 66Zn, 159Tb, and 208Pb Target Nuclei, *Braz. J. Phys.* **49** (2019) 760, https://doi.org/10.1007/s13538-019-00680-7.
13. G. R. Satchler and W.G. Love, Folding model potentials from realistic in- teractions for heavy-ion scattering, *Phys. Rep.* **55** (1979) 183, https://doi.org/10.1016/0370-1573(79)90081-4.
14. J. Cook, DFPOT-a program for the calculation of double folded potentials, *Commun. Comput. Phys.* **25** (1982) 125.
15. I.J. Thompson, Coupled reaction channels calculations in nuclear physics, *Comput. Phys. Rep.* **7** (1988) 167.
16. L. C. Chamon *et al.*, Toward a global description of the nucleus-nucleus in- teraction, *Phys. Rev. C* **66** (2002) 014610, https://doi.org/10.1103/PhysRevC.66.014610.
17. W. M. Seif and H. Mansour, Systematics of nucleon density distribu- tions and neutron skin of nuclei, *Int. J. Mod. Phys. E* **24** (2015) 1550083, https://doi.org/10.1142/S0218301315500834.
18. H. Schechter and L. F. Canto, Proximity formulae for folding potentials, *Nucl. Phys. A* **315** (1979) 470, https://doi.org/10.1016/0375-9474(79)90623-7.
19. S. A. Moszkowski, Energy dependence of the ion-ion potential with a simplified energy density method, *Nucl. Phys. A* **309** (1978) 273, https://doi.org/10.1016/0375-9474(78)90548-1.
20. C. W. De Jager, H. De Vries and C. De Vries, Nuclear charge- and magnetization-density-distribution parameters from elastic electron scattering, *At. Data Nucl. Data Tables* **14** (1974) 479, https://doi.org/10.1016/S0092-640X(74)80002-1.
21. C. Ngô *et al.*, Properties of heavy ion interaction potentials calculated in the energy density formalism, *Nucl. Phys. A* **252** (1975) 237, https://doi.org/10.1016/0375-9474(75)90614-4.
22. H. Ngô and C. Ngô, Calculation of the real part of the interaction potential between two heavy ions in the sudden approximation,*Nucl. Phys. A* **348** (1980) 140. https://doi.org/10.1016/0375-9474(80)90550-3.
23. R. K. Gupta, D. Singh and W. Greiner, Semiclassical and microscopic calculations of the spin-orbit density part of the Skyrme nucleus-nucleus interac- tion potential with temperature effects included, *Phys. Rev. C* **75** (2007) 024603, https://doi.org/10.1103/PhysRevC.75.024603.
24. O. N. Ghodsi and F. Torabi, Comparative study of fusion barriers using Skyrme interactions and the energy density functional, *Phys. Rev. C* **92** (2015) 064612, https://doi.org/10.1103/PhysRevC.92.064612.
25. R. K. Gupta, D. Singh, R. Kumar and W. Greiner, Universal func- tions of nuclear proximity potential for Skyrme nucleus-nucleus interaction in a semiclassical approach, *J. Phys. G: Nucl. Part. Phys.* **36** (2009) 075104, https://doi.org/10.1088/0954-3899/36/7/075104.

26. E. Wesolowski, The RMS radii of the charge distribution in nuclei, *J. Phys. G: Nucl. Part. Phys.* **11** (1985) 1401, https://doi.org/10.1088/0305-4616/11/8/008.
27. N. K. Dhiman, Role of Different Model Ingredients in the Exotic Cluster- Decay of 56Ni, Ukr. *J. Phys.* **57** (2012) 796, https://doi.org/10.15407/ujpe57.8.796.
28. http://www-nds.iaea.org/ripl-2.html.
29. S. Goriely, M. Samyn, P.-H. Heenen, J. M. Pearson and F. Tondeur, Hartree-Fock mass formulas and extrapolation to new mass data, *Phys. Rev. C* **66** (2002) 024326, https://doi.org/10.1103/PhysRevC.66.024326.
30. M. Samyn, S. Goriely, P.-H. Heenen, J. M. Pearson and F. Tondeur, A Hartree-Fock-Bogoliubov mass formula, *Nucl. Phys. A* **700** (2002) 142, https://doi.org/10.1016/S0375-9474(01)01316-1.
31. V. Hnizdo, J. Szymakowski, K. W. Kemper, and J. D. Fox, Folding-model description of elastic and inelastic scattering of 9Be by 40;44Ca and 39K at 40 MeV, *Phys. Rev. C* **24** (1981) 1495, https://doi.org/10.1103/PhysRevC.24.1495.
32. M. El-Azab Farid and M. A. Hassanain, Density-independent folding anal- ysis of the 6;7Li elastic scattering at intermediate energies, *Nucl. Phys. A* **678** (2000) 39, https://doi.org/10.1016/S0375-9474(00)00313-4.
33. G. Kocak, M. Karakoc, I. Boztosun and A. B. Balantekin, Effects of ff-cluster potentials for the 16O +16 O fusion reaction and S factor, *Phys. Rev. C* **81** (2010) 024615, https://doi.org/10.1103/PhysRevC.81.024615.
34. S. Qing-biao, F. Da-chun and Z. Yi-zhong, Neutron relativistic phe- nomenological and microscopic optical potential, *Phys. Rev. C* **43** (1991) 2773, https://doi.org/10.1103/PhysRevC.43.2773.
35. H. F. Ehrenberg, R. Hofstadter, U. Meyer-Berkhout, D.G. Ravenhall and S. E. Sobottka, High-Energy Electron Scattering and the Charge Distribution of Carbon-12 and Oxygen-16, *Phys. Rev.* **113** (1959) 666, https://doi.org/10.1103/PhysRev.113.666.
36. S. Hossain, M. N. A. Abdullah, Md. Z. Rahman, A. K. Basak and F. B. Malik, Non-monotonic potentials for 6Li elastic scattering at 88 MeV, *Phys. Scr.* **87** (2013) 015201, https://doi.org/10.1088/0031-8949/87/01/015201.
37. http://nrv.jinr.ru/nrv/
38. C. Y. Wong, Interaction Barrier in Charged-Particle Nuclear Reactions, *Phys. Rev. Lett.* **31** (1973) 766, https://doi.org/10.1103/PhysRevLett.31.766.
39. A. B. Balantekin and N. Takigawa, Quantum tunneling in nuclear fusion, *Rev. Mod. Phys.* **70** (1998) 77, https://doi.org/10.1103/RevModPhys.70.77.
40. Q. Haider and F. B. Malik, Barrier penetration calculation of heavy-ion fusion cross sections in the above- and sub-barrier regions, *J. Phys. G: Nucl. Phys.* **12** (1986) 537, https://doi.org/10.1088/0305-4616/12/6/012.
41. L. F. Canto, P. R. S. Gomes, J. Lubian, L. C. Chamon and E. Crema, Dy- namic effects of breakup on fusion reactions of weakly bound nuclei, *Nucl. Phys. A* **821** (2009) 51, https://doi.org/10.1016/j.nuclphysa.2009.02.001.
42. H. C. Manjunatha and K. N. Sridhar, Fusion barrier characteristics of actinides, *Nucl. Phys. A* **971** (2018) 83, https://doi.org/10.1016/j.nuclphysa.2018.01.016.
43. P. R. Christensen and A. Winther, The evidence of the ion-ion potentials from heavy ion elastic scattering, *Phys. Lett. B* **65** (1976) 19, https://doi.org/10.1016/0370-2693(76)90524-4.
44. D. G. Kovar *et al.*, Systematics of carbon- and oxygen-induced fusion on nuclei with $12 \leq A \leq 19$, *Phys. Rev. C* **20** (1979) 1305, https://doi.org/10.1103/PhysRevC.20.1305.
45. M. Ismail and M. M. Osman, Real part of the ion-ion interaction potential by use of the Negele realistic nucleon-nucleon force, *Phys. Rev. C* **24** (1981) 458, https://doi.org/10.1103/PhysRevC.24.458.
46. H. C. Manjunatha and K. N. Sridhar, Semi empirical formula for fusion barriers of nuclei with $1 \leq Z \leq 20$, *Indian J. Phys.* **95** (2021) 935, https://doi.org/10.1007/s12648-020-01756-w.
47. S. K. Gupta and S. Kailas, Rapid Communication Fusion barriers for heavy-ion systems, *Phys. Rev. C* **26** (1982) 747, https://doi.org/10.1103/PhysRevC.26.747.
48. M. Liu *et al.*, Applications of Skyrme energy-density functional to fu- sion reactions spanning the fusion barriers, *Nucl. Phys. A* **768** (2006) 80, https://doi.org/10.1016/j.nuclphysa.2006.01.011.
49. A. K. Mohanty, S. V. S. Sastry, S. K. Kataria and V. S. Ramamurthy, Experimental determination of energy-dependent barriers for fusion, *Phys. Rev. C* **46** (1992) 2012, https://doi.org/10.1103/PhysRevC.46.2012.